Heterogeneous & Homogeneous & Bio-

CHEMCATCHEM

CATALYSIS

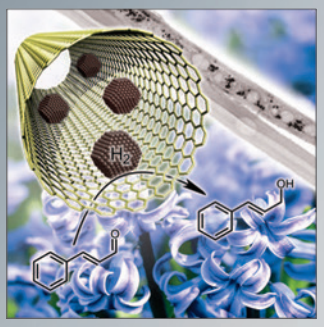

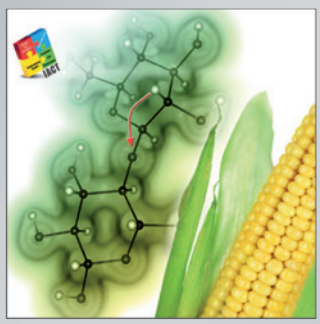

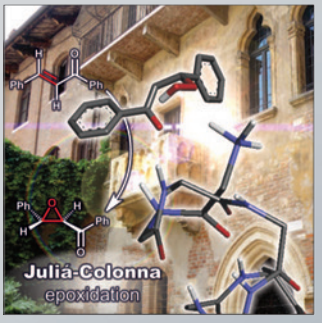

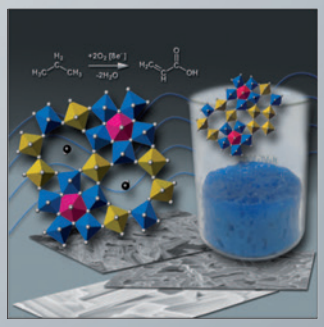

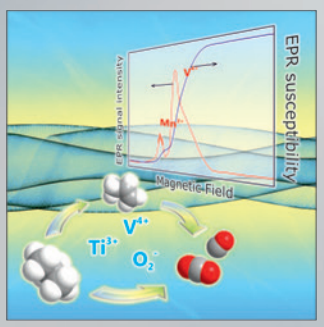

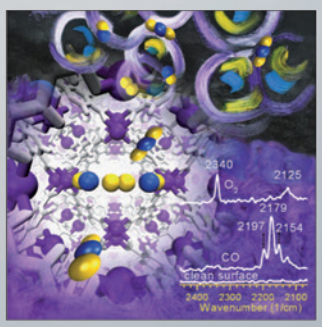

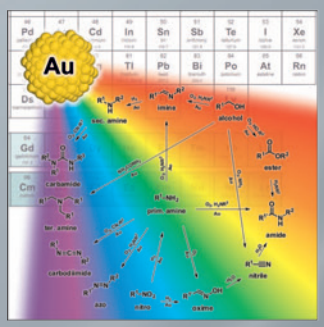

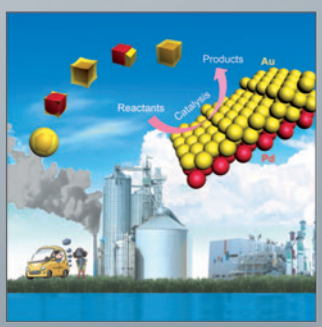

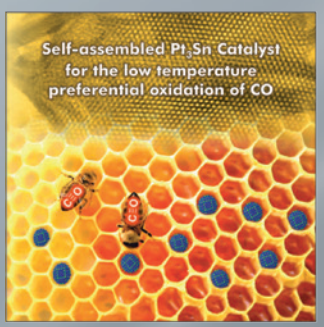

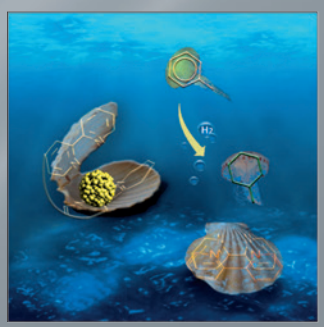

Reprint

A Journal of

ChemPubSoc Europe

WILEY-VCH

www.chemcatchem.org

ChemPubSoc Europe

DOI: 10.1002/cctc.201801545

CHEMCATCHEM Full Papers

Influence of Carbon and Oxygen Chemical Potentials on the Hydrogen Donor Identity During Methanation on Ni, Co, and Ni-Co Clusters

Petar T. Lachkov[a] and Ya-Huei (Cathy) Chin*[a]

Rate measurements in the kinetically controlled regime and equilibrium carbon and oxygen chemical titrations show two distinct mechanistic paths during CO_x methanation reactions on first-row transition metal clusters. On Ni and, for a limiting set of conditions, Ni–Co clusters, the reaction occurs via the addition of a hydrogen adatom into CH_3* intermediates on clusters partially covered with carbon. On Co and, in a subset of conditions, Ni–Co clusters, it occurs via the donation of hydrogen from OH* to CH_3* on clusters partially covered with reactive oxygen adatoms (O*). The $[CO]^2$-to-$[CO_2]$ and $[CO_2]$-to-[CO] operating ratios are the surrogates of carbon and oxygen chemical potentials, respectively, as a consequence of water-gas shift equilibration. These ratios, together with the carbon and oxygen binding energies, determine the relative surface coverages of carbon and oxygen, the involvement of H* vs. OH* in the kinetically-relevant step, and in turn, the rate dependencies. Stronger carbon and oxygen binding energies lead to more stabilized transition states of the kinetically relevant steps and larger methanation rates.

Introduction

Reactions between hydrogen and carbon oxides (monoxide or dioxide) on first-row transition metals at low pressures and moderate temperatures (e.g., 1 atm, 573–973 K) evolve methane[1–3] and, as the pressure elevates and temperature decreases (e.g., 5–20 atm, 423–573 K), form higher alkanes.[4,5] The former reaction that forms methane is useful for the removal of CO_x ($x=1$ or 2) from H_2 rich streams[6,7] and direct synthesis of CH_4[1,2] and involves the following concomitant reactions (Equations 1a–1d):

$$2CO + 2H_2 \leftrightarrow CH_4 + CO_2 \quad \Delta H_r^{\circ}{}_{298\,K} = -247\,kJ\,mol^{-1} \tag{1a}$$

$$CO + 3H_2 \leftrightarrow CH_4 + H_2O \quad \Delta H_r^{\circ}{}_{298\,K} = -206\,kJ\,mol^{-1} \tag{1b}$$

$$CO_2 + H_2 \leftrightarrow CO + H_2O \quad \Delta H_r^{\circ}{}_{298\,K} = 41\,kJ\,mol^{-1} \tag{1c}$$

$$2CO \leftrightarrow CO_2 + C\ (graphite) \quad \Delta H_r^{\circ}{}_{298\,K} = -172\,kJ\,mol^{-1} \tag{1d}$$

Equations 1a and 1b are the methanation reactions, which are also the reverse of methane reforming reactions that form synthesis gas;[8,9] Equation 1c is the reverse water-gas shift reaction and Equation 1d is the Boudouard reaction. Group VIII transition metals such as Ni,[6,7,10–15] Fe,[6,12,15,16] Co,[12,14,17] Ru,[12,18–20] Rh,[12,18] Pd,[12,18] and Pt[12,17,18] catalyze these reactions effectively. Among these metals, first-row transition metals, especially Ni, are attractive catalyst elements, because they are earth abundant and therefore available at low cost. Ni catalysts, however, bind to carbonaceous intermediates strongly and thus suffer from severe coking via routes such as the Boudouard reaction (Equation 1d). The carbon deposition, which involves initial carbon nucleation and sequential carbon growth on metal surfaces, causes active site blocking and thus inhibits catalytic turnovers.[10,21] Temperature programmed oxidation (TPO) studies[2] and Auger Electron Spectroscopic (AES) analyses[10] of the carbon species on spent Ni single crystal surfaces, after exposure to CO and H_2 mixtures, showed significant carbon deposition covering up to 0.25 ML of Ni(100) surfaces. In designing more stable, earth-abundant Ni based catalysts, preventing coke formation has remained as a major challenge.

The reaction mechanism for methanation on transition metals is straight forward. It involves the initial H_2 and CO activation on metal cluster surfaces, followed by two plausible, competitive pathways that form either CH_4 or coke.[8–10,21] The first route that evolves CH_4 begins with an initial H_2 activation, followed by successive H* addition events into CO* (where * denotes a metal site) to form HCO* and HCOH* intermediates, and finally a C–O bond cleavage step.[2,22,23] This H*-assisted C–O activation pathway is energetically more favorable than the direct C–O scission of CO*, as evidenced by (1) the smaller activation barriers calculated with density functional theory {59–261 kJ mol^{-1} smaller for the C–O activation in HCOH* than in CO* on Ni(211),[2] Fe(110),[22] Co(0001),[22] and Ru(111) terraces of Ru_{201} clusters[23]} and (2) rate dependencies consistent with this mechanistic proposal on Fe clusters promoted with Zn, Cu, and K.[22] The second, competitive route that forms coke requires the dissociation of carbonaceous intermediates to carbon adatoms (e.g., CO* to C* and O* or CH* to C* and H*).[8,9,22] These carbon, oxygen, and hydrogen adatoms adsorb on and compete for active sites at cluster surfaces, thus the

[a] P. T. Lachkov, Prof. Y.-H. (. Chin
Department of Chemical Engineering and Applied Chemistry
University of Toronto
200 College St.
Toronto, ON M5S 3E5 (Canada)
E-mail: cathy.chin@utoronto.ca

Supporting information for this article is available on the WWW under https://doi.org/10.1002/cctc.201801545

differences between the C, O, and H binding strengths influence largely the coverages of the various species at cluster surfaces. However, hydrogen adatoms (H*) bind much more weakly than carbon (C*) and oxygen (O*) adatoms on first-row Group VIII transition metals [e.g., binding energies (energy released during bond formation) range from −289 to −276 kJ $(\text{mol H})^{-1}$ vs. −714 to −496 kJ $(\text{mol O})^{-1}$ and −769 to −629 kJ $(\text{mol C})^{-1}$ relative to gaseous H, O, and C atoms, respectively, on close-packed surfaces[24,25]] thus these metal surfaces remain free of H* adsorbates during methanation catalysis.

These previous studies have led us to design an earth-abundant catalyst that is effective for hydrogen addition and ineffective for carbon nucleation and coke formation. Herein, we report the forward rates of CH_4 formation during CO_x–H_2 reactions on monometallic Ni and Co clusters and bimetallic Ni–Co alloy clusters, in the kinetically controlled regime and after reaching steady-state, when rates remain unchanged with time. On these clusters, we show a dynamic transition in surface intermediates from reactive carbon to oxygen species and a concomitant switch in the reaction mechanism as we increase the difference between the carbon and oxygen binding strengths, by altering their chemical compositions. On Ni and, under selected conditions, on Ni–Co clusters, CH_4 formation occurs via a kinetically relevant hydrogen addition from H* to CH_3*, when clusters are partially covered with carbon. On the other hand, on Co and, under selected conditions, on Ni–Co clusters, kinetically relevant hydrogen addition, which transfers the hydrogen from OH* to CH_3* on clusters partially covered with oxygen, prevails. We further rationalize the mechanistic transition among the metal/alloy, by connecting it to the difference in the carbon and oxygen binding strengths in each of the metals, ΔBE_{C-O}, as Equation 2:

$$\Delta BE_{C-O} = BE_C - BE_O \quad (2)$$

where BE_C and BE_O are the binding energies for C* and O*, respectively, on their respective closed-packed terrace. This ΔBE_{C-O} reflects the relative affinity of a metal/alloy surface towards carbon and oxygen. Together with the $[CO]^2$-to-$[CO_2]$ and $[CO_2]$-to-[CO] pressure ratios, the ΔBE_{C-O} value sets the relative chemical potentials of carbon and oxygen at the cluster surfaces during steady-state catalysis and, in turn, dictates the relative coverages of the various carbon and oxygen containing species, identity of the most abundant reactive intermediates, identity of the H donor for CH_4 formation, and overall rate dependencies. For this reason that is unrecognized previously, the ΔBE_{C-O} and the operating CO and CO_2 pressures determine the resulting catalytic rates and stability against coke deposition on Ni, Co, and Ni–Co clusters. We show that incorporating Co into Ni clusters increases their CO_x methanation rate coefficients because of the much stronger C* and O* binding energies for Co than Ni, which lead to more exothermic adsorptions of the CH_3* and H* or the CH_3* and OH* reactant precursors as well as to more stabilized transition states for the kinetically relevant CH_4 formation steps. Finally, Co clusters lead to the largest and most stable CH_4 rate coefficients compared to Ni–Co and Ni, due to the stronger affinity of Co relative to Ni towards binding to O* instead of C*, as O* removes and oxidizes C* more effectively and increases the catalyst stability.

Results and Discussion

Removal of Rate Corruptions Caused by Heat and Mass Transports, Thermodynamics, and Time-Dependent Carbon Deposition During CO_x Methanation on Co, Ni–Co, and Ni Clusters

CO_x ($x = 1$–2) and H_2 reactions proceed via the series of reactions described in Equations 1a–1d. The reverse water-gas shift reaction (RWGS, Eqn. 1c) is mildly endothermic (+41 kJ mol^{-1}), whereas the CO methanation reactions that form CH_4 together with either CO_2 (Eqn. 1a) or H_2O (Eqn. 1b) as well as the Boudouard reaction (Eqn. 1d) are highly exothermic (−172 to −247 kJ mol^{-1}). These latter reactions (Eqns. 1a, 1b, and 1d) may cause significant temperature and concentration gradients within the individual catalyst particles and along the catalyst bed, which in turn could corrupt the rate data assessments and interpretation. The lack of dilution effects on turnover rates, detailed in Section S1 of the Supporting Information, rigorously confirms the complete removal of all temperature and concentration gradients.

Next, we examine the extents of the various reactions and their deviation from chemical equilibrium during rate measurements. The approach-to-equilibrium for the RWGS reaction (η_{RWGS}, Equation 3) is:

$$\eta_{RWGS} = \frac{Q_{RWGS}}{K_{RWGS}} \quad (3)$$

where Q_{RWGS} is the reaction quotient and K_{RWGS} is the equilibrium constant for the RWGS reaction (Eqn. 1c). Figure 1a shows the η_{RWGS} values with 3–19 kPa CO_2 and 24–82 kPa H_2 for the three catalysts (Co, Ni–Co, Ni) at 873 K. The η_{RWGS} values remain at near unity within the limit of experimental error (1.00 ± 0.12), thus the RWGS reaction attains chemical equilibrium and the RWGS thermodynamics dictate the relative concentrations of CO_2, H_2, CO, and H_2O in the reactor effluent (Equation 4):

$$K_{RWGS} = \left(\frac{[CO][H_2O]}{[CO_2][H_2]}\right)_{eq} = \left(\frac{[CO][H_2O]}{[CO_2][H_2]}\right)_{reactoreffluent} \quad (4)$$

where [X] represents the gas phase pressure of species X, and subscripts *eq* and *reactor effluent* denote chemical equilibrium and reactor effluent stream, respectively.

We examine also the extent of the concomitant methanation reactions (Eqns. 1a and 1b), which are highly exothermic and may become limited by thermodynamics, at 873 K. The approach-to-equilibrium for the CH_4 evolution reaction in Equation 1a ($\eta_{CH_4,1a}$) is shown in Equation 5:

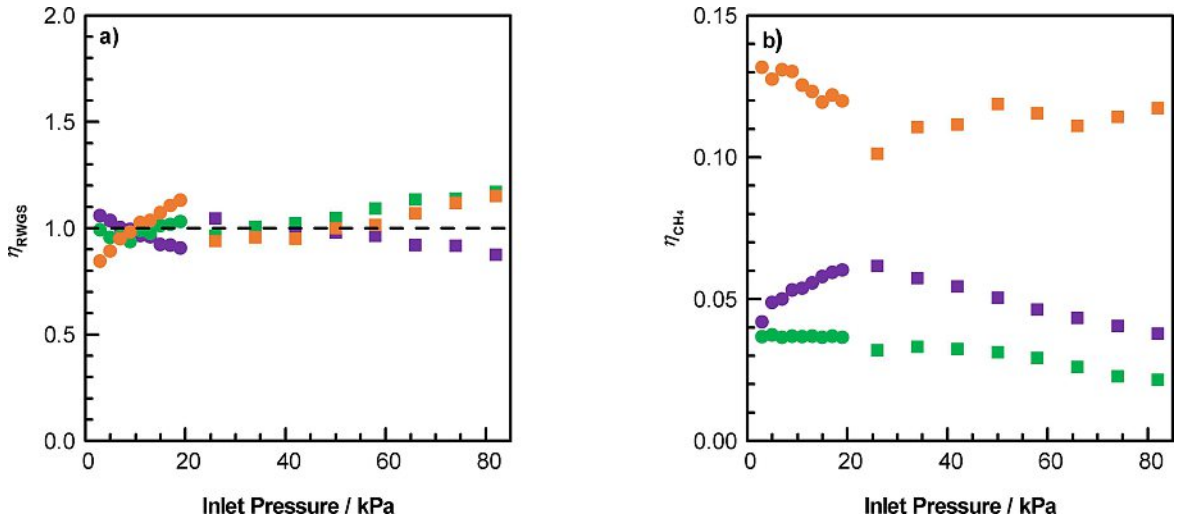

Figure 1. Approach-to-equilibrium for (a) reverse water-gas shift (η_{RWGS}) and (b) CO_x methanation ($\eta_{CH_4,1a}$) reactions during steady-state H_2-CO_2 reactions on dispersed 26–30 nm Ni (●, ■), Ni–Co (●, ■), and Co (●, ■) clusters (12 g-atom% metal dispersed on MgO-ZrO_2) as a function of the CO_2 (at 50 kPa H_2, ●, ●, ●) or H_2 (at 10 kPa CO_2, ■, ■, ■) inlet pressures at 873 K (7–14×10^5 $cm^3 g_{cat}^{-1} h^{-1}$, 10 ZrO_2:catalyst intra-pellet and 100 SiO_2:catalyst inter-pellet dilution ratios).

$$\eta_{CH_4,1a} = \frac{Q_{CH_4,1a}}{K_{CH_4,1a}} \quad (5)$$

where $Q_{CH_4,1a}$ is the reaction quotient and $K_{CH_4,1a}$ is the equilibrium constant for the methanation reaction (Eqn. 1a). The approach-to-equilibrium for the CH_4 evolution reaction in Equation 1b, $\eta_{CH_4,1b}$, is the product of $\eta_{CH_4,1a}$ and η_{RWGS}, because Equation 1b is the sum of Equations 1a and 1c. Since η_{RWGS} equals unity (1.00±0.12), $\eta_{CH_4,1b}$ and $\eta_{CH_4,1a}$ have identical values. Figure 1b shows the $\eta_{CH_4,1a}$ values during reactions with 3–19 kPa CO_2 and 24–82 kPa H_2 feed mixtures on dispersed 26–30 nm Co, Ni–Co, and Ni clusters at 873 K. The $\eta_{CH_4,1a}$ values range from 0.02 to 0.13, indicating that the methanation reactions (both Equations 1a and 1b) are nearly irreversible and far away from chemical equilibrium for all catalysts. These $\eta_{CH_4,1a}$ values, which equal to $\eta_{CH_4,1b}$, taken together with the net CH_4 site-time-yields ($r_{CH_4,net}$), give the forward CH_4 site-time-yields ($r_{CH_4,f}$) per exposed metal atom (Equation 6):

$$r_{CH_4,f} = \frac{r_{CH_4,net}}{1 - \eta_{CH_4,1a}} \quad (6)$$

Figure S2 in the Supporting Information shows the forward CH_4 site-time-yields on Co, Ni–Co, and Ni catalysts (26–30 nm average cluster diameter) as a function of time-on-stream at 873 K. The CH_4 site-time-yields on Ni, Ni–Co, and Co catalysts decrease by 65, 80, and 20% from their initial values for the first 80, 100, and 20 h, respectively, after which they remain constant throughout the kinetic experiments (<10% deviation over the course of 40 h). These decreases in site-time yields may arise from changes in active site density, as carbon deposits on cluster surfaces. These deactivation profiles indicate that Co clusters are the most stable and resistant to carbon deposition. Due to the catalyst deactivation, we carried out thorough kinetic measurements on Ni, Ni–Co, and Co catalysts after contacting them to reaction mixtures for at least 80, 100, and 20 h, respectively, after which the rates remained essentially unchanged (±10%).

These above results, taken together, confirm that the CH_4 site-time-yields and their interpretation reported herein are free of corruptions from heat and mass transport, thermodynamics, and site density changes. Next, we probe the C* and O* coverages on the Ni, Ni–Co, and Co clusters as they contact to CO–CO_2 mixtures and correlate these coverages to their thermodynamic parameters, namely the binding energies of carbon (BE_C), oxygen (BE_O), and their difference (ΔBE_{C-O}), and the operating [CO_2]-to-[CO] and [CO]^2-to-[CO_2] pressure ratios.

The [CO_2]-to-[CO] and [H_2O]-to-[H_2] Pressure Ratios are Rigorous Surrogates of the Oxygen Chemical Potential on Ni, Ni–Co, and Co Clusters

We probe the relationships between the partial pressures of methanation reactants and products and the coverages of oxygen and carbonaceous intermediates at cluster surfaces during steady-state catalysis. Steps 1–5 of Scheme 1 are the proposed elementary steps for the RWGS reaction (Eqn. 1c). Since the RWGS reaction is at chemical equilibrium (Figure 1a), each of these elementary steps must also attain chemical equilibrium. The reaction begins with the dissociative adsorption of CO_2 onto bare metal site pairs (*–*), forming O* and CO* (Step 1), the latter then desorbs as CO (Step 2). H_2 dissociatively adsorbs as H* adatoms on a metal site pair (Step 3). One of the H* adatoms reacts with O* to produce OH*, which then recombines with another OH* to desorb as H_2O, leaving an O* adatom behind (Steps 4–5). The surface oxygen-to-vacant site ratio, [O*]/[*] (Equation 7a), derived from quasi-equilibrium assumptions, is:

Pathway	Step	Elementary Reaction	Rate or Equilibrium Constant
RWGS	1	$CO_2 + * + * \rightleftharpoons CO^* + O^*$	K_1
	2	$CO^* \rightleftharpoons CO + *$	K_2
	3	$H_2 + 2^* \rightleftharpoons 2H^*$	K_3
	4	$H^* + O^* \rightleftharpoons OH^* + *$	K_4
	5	$2OH^* \rightleftharpoons H_2O + O^* + *$	K_5
C Deposition	6	$CO^* + * \rightleftarrows C^* + O^*$	$k_{6,f}$, $k_{6,r}$, K_6
Methanation A	7A	$CO^* + H^* \rightleftharpoons HCO^* + *$	K_{7A}
	8A	$HCO^* + H^* \rightleftharpoons HCOH^* + *$	K_{8A}
	9	$HCOH^* + * \rightleftharpoons CH^* + OH^*$	K_9
	10A	$CH^* + * \rightleftarrows C^* + H^*$	$k_{10A,f}$, $k_{10A,r}$, K_{10A}
	11A	$CH^* + H^* \rightleftharpoons CH_2^* + *$	K_{11A}
	12A	$CH_2^* + H^* \rightleftharpoons CH_3^* + *$	K_{12A}
	13A	$CH_3^* + H^* \rightleftharpoons CH_4 + * + *$	$k_{13A,f}$, $k_{13A,r}$, K_{13A}
Methanation B	7B	$CO^* + OH^* \rightleftharpoons HCO^* + O^*$	K_{7B}
	8B	$HCO^* + OH^* \rightleftharpoons HCOH^* + O^*$	K_{8B}
	9	$HCOH^* + * \rightleftharpoons CH^* + OH^*$	K_9
	10B	$CH^* + O^* \rightleftarrows C^* + OH^*$	$k_{10B,f}$, $k_{10B,r}$, K_{10B}
	11B	$CH^* + OH^* \rightleftharpoons CH_2^* + O^*$	K_{11B}
	12B	$CH_2^* + OH^* \rightleftharpoons CH_3^* + O^*$	K_{12B}
	13B	$CH_3^* + OH^* \rightleftharpoons CH_4 + * + O^*$	$k_{13B,f}$, $k_{13B,r}$, K_{13B}
Surface O	I	$CO_2 + * \rightleftharpoons CO + O^*$	K_I
Or C	II	$H_2O + * \rightleftharpoons H_2 + O^*$	K_{II}
Formation	III	$O_2 + 2^* \rightleftharpoons 2O^*$	K_{III}
	IV	$nC^* \rightleftharpoons nC(graphite) + n^*$	K_{IV}
	V	$2CO + * \rightleftharpoons C^* + CO_2$	K_V

Scheme 1. A proposed sequence of elementary steps during reverse water-gas shift, methanation, and Boudouard reactions on 26–30 nm Ni, Ni–Co, and Co clusters ($\rightleftharpoons$ denotes a quasi-equilibrated step, $\rightleftarrows$ a reversible step, and $\rightleftharpoons$ a reversible rate-limiting step. K_j is the equilibrium constant, $k_{j,f}$ is the forward rate constant, and $k_{j,r}$ is the reverse rate constant for the respective elementary step, *j*).

$$\frac{[O^*]}{[*]} = K_1K_2\frac{[CO_2]}{[CO]} = K_I\gamma_O = \frac{1}{K_3K_4^2K_5}\frac{[H_2O]}{[H_2]} = K_{II}\gamma_H \quad (7a)$$

$$\text{where } \gamma_O = \frac{[CO_2]}{[CO]} \quad (7b)$$

$$\text{and } \gamma_H = \frac{[H_2O]}{[H_2]} \quad (7c)$$

where K_j is the equilibrium constant for elementary Step *j* in Scheme 1, K_I and K_{II} are the equilibrium constants for O* formation during CO_2 and H_2O dissociation, respectively (Steps I and II, $K_I = K_1K_2$, $K_{II} = K_3^{-1}K_4^{-2}K_5^{-1}$), and γ_O and γ_H equal to the $[CO_2]$-to-[CO] and $[H_2O]$-to-$[H_2]$ pressure ratios, respectively. The [O*]/[*] ratio is proportional to the $[CO_2]$-to-[CO] pressure ratio (γ_O), and alternatively, to the $[H_2O]$-to-$[H_2]$ pressure ratio (γ_H), because the RWGS reaches chemical equilibrium and the equilibrium expression relates the two pressure ratios according to Equation 4 (where $K_{RWGS} = K_IK_{II}^{-1} = K_1K_2K_3K_4^2K_5$). The [O*]/[*] ratio also relates to the oxygen virtual pressure, $[O_2]_{virtual}$, a fictitious but quantifiable O_2 pressure, that by definition[26,27] is in chemical equilibrium with the surface oxygen contents via the O_2 adsorption-desorption reaction (Step III, Scheme 1) and is the rigorous surrogate of the oxygen chemical potential (Equation 8):

$$\frac{[O^*]}{[*]} = \sqrt{K_{III}[O_2]_{virtual}} = K_I\gamma_O = K_{II}\gamma_H \quad (8)$$

Oxygen uptake measurements probe and then confirm that γ_O indeed dictates the O* coverages, $[O_2]_{virtual}$, and oxygen chemical potential. Figure 2 shows the equilibrium oxygen uptakes as fractional oxygen coverages, O_s/M_s (where *s* denotes surface metal atoms), as a function of the γ_O and γ_H pressure ratios, measured by contacting the Co, Ni–Co, and Ni clusters to CO_2–CO mixtures with varying γ_O ratios (0.24 to 32) at 873 K. For each catalyst, the O_s/M_s ratios depend strictly on γ_O and γ_H, the pressure ratios given in Equations 7b and 7c, respectively, irrespective of the individual CO_2 and CO or H_2O and H_2 pressures. For Co clusters, which have an O* binding energy of −550 kJ mol^{-1} at their (111) surfaces,[24] the O_s/M_s ratio is 0.58 at

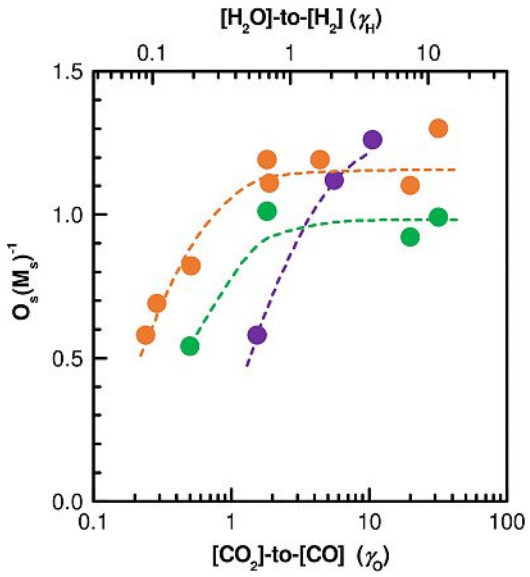

Figure 2. Equilibrium oxygen uptakes, expressed as the surface oxygen-to-surface metal atomic ratios (O_s/M_s), as a function of the operating $[CO_2]$-to-[CO] (γ_O) and $[H_2O]$-to-$[H_2]$ (γ_H) ratios, after exposure to CO–CO_2 mixtures for 2 h at 873 K on 30 nm Co (●), 27 nm Ni–Co (●), and 26 nm Ni (●) clusters (12 g-atom% metal on MgO-ZrO_2).

a γ_O value of 0.24 and then increases to above a monolayer, reaching 1.2 for γ_O values above 2. Ni–Co alloy clusters bind to O* more weakly than Co clusters with an O* binding energy of −523 kJ mol^{-1} at their (111) surfaces.[24] On these Ni–Co clusters, the O_s/M_s ratios are smaller than those on Co, i.e., 0.54 on Ni–Co vs. 0.82 on Co when γ_O equals 0.50 ± 0.01; they also increase to about a monolayer when γ_O rises above 2. Comparing to Co and Ni–Co clusters, Ni clusters have the weakest O* binding energy of −496 kJ mol^{-1} at their (111) surfaces[24] and their O_s/M_s ratios increase to 1.3 at the largest γ_O values. Among these three clusters, the O_s/M_s ratios increase to their maximum values at γ_O values of 1.8, 1.9, and more than 10 on Co, Ni–Co, and Ni, respectively, a trend that parallels their decrease in O* binding energy,[24] which leads to larger K_I or K_{II} values (Eqn. 7a) on Co than on Ni–Co and Ni clusters. These oxygen uptakes show that the O* coverages are functions of the operating γ_O and related γ_H values. This direct dependence of O* coverages to γ_O basically means that the operating $[CO_2]$-to-[CO] and the related $[H_2O]$-to-$[H_2]$ ratios are both the rigorous surrogates of oxygen chemical potential at metal cluster surfaces, as captured by Equation 7a.

The $[CO]^2$-to-$[CO_2]$ Pressure Ratio is a Rigorous Surrogate of the Carbon Chemical Potential on Ni, Ni–Co, and Co Clusters

Scheme 1 also outlines steps related to carbon deposition, including those of the Boudouard reaction (Eqn. 1d). Specifically, Steps 2 and 6–13 describe the steps that lead to the formation of surface carbon intermediates. In the direct C–O cleavage route,[8,9,22] CO adsorbs (reverse of Step 2) and dissociates into C* and O* adatoms (Step 6). Carbonaceous deposits also form from CH_4 via the microscopically reverse pathway of Scheme 1, as proposed in reforming reactions on supported Ni,[8,9] Ni–Co,[9] and Co[9] clusters. These CH_4 decomposition reactions involve sequential C–H cleavages that occur either unassisted on *–* site pairs or assisted by O* on O*–* site pairs to form C* and H* in the reverse of Steps 10*i*–13*i* (*i* equals either A or B for cluster surfaces free of O* or partially covered with O*, respectively).[9] This C–H cleavage pathway also occurs during methanation reactions after hydrogen additions into CO* that form HCOH* in Steps 7*i*–8*i*, followed by C–O cleavage that forms CH* in Step 9.[2,22,23] Therefore, these two C–O (Step 6) and C–H (Steps 7–10) cleavage routes determine the surface carbonaceous contents.

We postulate that during CH_4 formation, the final H addition onto CH_3* (Step 13*i*) is kinetically relevant, and consequently, the H assisted C–O bond cleavage and all prior H additions into CO are quasi-equilibrated (Steps 7*i*–8*i*, 9, 11*i*–12*i*). The H donors for these reactions are either H* or OH*, which form during H_2 dissociation on clusters free of O* (Step 3) or via the RWGS pathway on clusters partially covered with O* (Steps 3–4). Finally, C* adatoms nucleate and then form bulk graphitic carbon (Step IV), completing the pathway for the Boudouard reaction (Eqn. 1d). Pseudo steady-state balances on the C* formation and consumption steps, i.e., forward and reverse of Steps 6 and 10, describe the C* coverages, given here in terms of the atomic ratio of carbon-to-vacant site, [C*]/[*], at the cluster surfaces (Equation 9):

$$\frac{[C^*]}{[*]} = \frac{\frac{k_{6,f}}{K_2}[CO] + k_{10i,f}K_1^nK_2^{n-1}K_3^{0.5}K_4^{2n+1}K_{7i}K_{8i}K_9\frac{[CO]^{1-n}[H_2]^{0.5}}{[CO_2]^{-n}}}{k_{6,r}K_1K_2\frac{[CO_2]}{[CO]} + k_{10i,r}K_1^{n+1}K_2^{n+1}K_3^{0.5}K_4^{n+1}\frac{[CO_2]^{n+1}[H_2]^{0.5}}{[CO]^{n+1}}} \quad (9)$$

where $k_{j,f}$ and $k_{j,r}$ are the forward and reverse rate constants, respectively, for elementary Step *j* in Scheme 1. For the case in which cluster surfaces are free of O* and contain vacant sites as well as some C*, subscript *n* equals −1. For the alternative case in which cluster surfaces are partially covered with O* and free of C*, subscript *n* equals 0. As shown in Equation 9, the [C*]/[*] ratio relates to the CO, CO_2, and H_2 pressures. We note that this expression captures all the operating regimes and surface coverages, ranging from cluster surfaces containing predominantly O* intermediates, to vacant sites, and then to C* coverages up to a monolayer. The expression, however, does not capture those conditions that lead to multiple carbon layers, carbon solvation into the cluster bulk, and the growth of carbon whiskers.

DFT calculations on Ni(211),[28] Ni(111),[29] and Co(0001)[22] surfaces covered with either 0.5 ML CO* or CH* show that C* formation and consumption via the C–H cleavage and recombination pathways in Step 10 are much more favorable, since their activation barriers for the forward and reverse reactions are 75–154 kJ mol^{-1} smaller than those for the C–O cleavage and recombination pathways in Step 6. Thus, the pathway involving H assisted C–O cleavage followed by C–H cleavage (Steps 7–10) is the preferred route for C* formation since it is the minimum energy path. As a result, the forward rate constant for Step 6 is much smaller than that for Step 10*i* ($k_{6,f} \ll k_{10i,f}$); similarly, the reverse rate constant for Step 6 is also much smaller than that of Step 10*i* ($k_{6,r} \ll k_{10i,r}$). As a result, Equation 9 simplifies to Equation 10a:

$$\frac{[C^*]}{[*]} = \frac{K_4^nK_{7i}K_{8i}K_9K_{10i}}{K_1K_2^2}\frac{[CO]^2}{[CO_2]} = K_V\gamma_C \quad (10a)$$

$$\text{where } \gamma_C = \frac{[CO]^2}{[CO_2]} \quad (10b)$$

where K_{10i} is the equilibrium constant for Step 10*i*, which by definition is the ratio of the forward rate constant to the reverse rate constant of that step ($k_{10i,f}k_{10i,r}^{-1}$), and K_V is the equilibrium constant for C* formation during CO dissociation (Step V) ($K_V = K_1^{-1}K_2^{-2}K_4^nK_{7i}K_{8i}K_9K_{10i}$). Equation 10a relates the [C*]/[*] ratio, which is the direct manifestation of the carbon chemical potential at cluster surfaces during steady-state catalysis, to γ_C, the operating $[CO]^2$-to-$[CO_2]$ pressure ratio, as defined in Equation 10b.

Temperature programmed oxidation (TPO) experiments quantify the amount of carbon deposits on the catalysts and confirm the direct relationship between [C*]/[*] ratios and γ_C values. Figure 3 shows the measured carbon uptakes as fractional carbon coverages, after exposing the Co, Ni–Co, and Ni catalysts to CO-CO_2 mixtures at different operating $[CO]^2$-to-

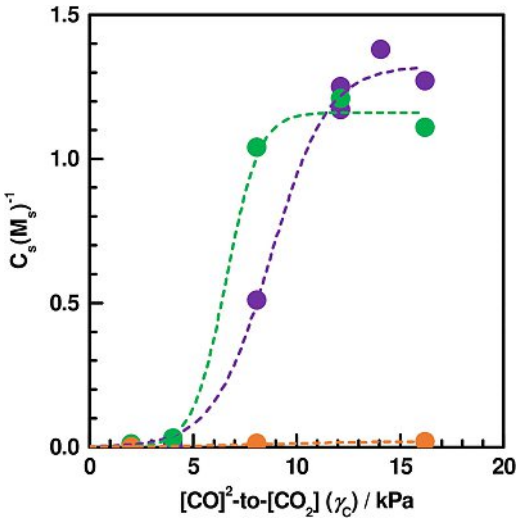

Figure 3. Equilibrium carbon uptakes, expressed as the surface carbon-to-surface metal atomic ratios (C_s/M_s), as a function of the operating $[CO]^2$-to-$[CO_2]$ (γ_C) ratios following exposure of 30 nm Co (●), 27 nm Ni–Co (●), and 26 nm Ni (●) clusters (12 g-atom% metal on MgO–ZrO_2) to CO–CO_2 mixtures for 4 h at 873 K.

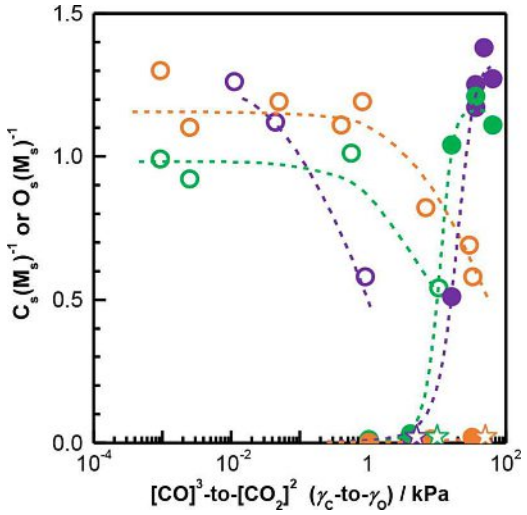

Figure 4. Equilibrium oxygen (○, ○, ○) and carbon (●, ●, ●) uptakes, expressed as the ratio of either oxygen or carbon to surface metal atoms (O_s/M_s or C_s/M_s), plotted as a function of the operating $[CO]^3$-to-$[CO_2]^2$ (γ_C-to-γ_O) ratios following exposure of 30 nm Co (○, ●), 27 nm Ni–Co (○, ●), and 26 nm Ni (○, ●) clusters (12 g-atom% metal on MgO-ZrO_2) to CO–CO_2 mixtures for 2–4 h at 873 K. Transition points from O* to C* covered Ni (☆), Ni–Co (☆), and Co (☆) cluster surfaces.

$[CO_2]$ ratios (2–16 kPa) at 873 K. The carbon uptakes, expressed in terms of the carbon-to-metal atomic ratios at cluster surfaces (C_s/M_s), are functions of γ_C, regardless of the individual CO and CO_2 pressures. These carbon uptakes and their dependence with γ_C confirm that γ_C completely prescribes and dictates the instantaneous C* coverages on metal cluster surfaces, according to Equation 10a, and therefore is a rigorous surrogate of the carbon chemical potentials. For Ni and Ni–Co, the C_s/M_s values increase rather abruptly from zero to 1.25 ± 0.1, reflecting that the carbon coverages grow from uncovered to saturated, when the γ_C and carbon chemical potential exceed a critical value. On Ni clusters that have a C* binding energy of $-629\ kJ\,mol^{-1}$ at their (111) surfaces,[24] the C_s/M_s ratios increase from 0.01 to above a monolayer ($C_s/M_s = 1.3$), as γ_C increases from 2 to 16 kPa. C_s/M_s ratios on Ni–Co clusters, which bind to C* more strongly with a binding energy of $-649\ kJ\,mol^{-1}$ on their (111) surfaces,[24] also increase with increasing γ_C, i.e., from 0.01 to 1.2, as γ_C increases from 2 to 12 kPa. Finally, C_s/M_s ratios on Co clusters remain below 0.02 for all γ_C values (2–16 kPa), despite their strong binding to C* of $-668\ kJ\,mol^{-1}$ on (111) surfaces,[24] likely because surface O* adatoms effectively react with and remove the C* adsorbates, as confirmed by comparing the C* and O* coverages in Figure 4.

The ratio of carbon-to-oxygen chemical potential, γ_C-to-γ_O, is $[CO]^3$-to-$[CO_2]^2$, derived from dividing Equations 10b by 7b. This ratio determines the relative coverages of carbon-to-oxygen, as illustrated in Figure 4 for Ni, Ni–Co, and Co clusters. At low γ_C-to-γ_O ratios (e.g., 0.01–1 kPa for Ni), the clusters are covered nearly exclusively by O*; in contrast, at high γ_C-to-γ_O ratios (e.g., 10–100 kPa for Ni), O* species are being removed and C* species become the dominant surface intermediates. On these clusters, the identity of the most abundant surface intermediate (MASI) appears to undergo a dynamic transition from O* to C* at the γ_C-to-γ_O ratios of 5, 10, and 50 kPa on Ni, Ni–Co, and Co clusters, respectively, as indicated on the figure. This trend parallels the decrease in the difference between their carbon and oxygen binding energies, ΔBE_{C-O} (Eqn. 2), from -133, -126, and $-118\ kJ\,mol^{-1}$ for Ni, Ni–Co, and Co, respectively, an indication that clusters prefer binding to O* instead of C* as ΔBE_{C-O} becomes less negative. Next, we report the different kinetic manifestations of O* and C* coverages and their dynamic transition and then interpret these phenomena in terms of the chemical potentials of oxygen and carbon at cluster surfaces.

Rate Expression for Methanation Reactions on Ni, Ni–Co, and Co Clusters Partially Covered with Reactive C* and O* Intermediates

There are two parallel pathways (Pathways A and B of Scheme 1) that convert CO_x and H_2 to CH_4, depending on the identity of H donor involved in the successive H addition steps. In Pathway A, CO* undergoes sequential H* addition events, forming HCO* and then HCOH* (Steps 7A and 8A). Here, metal surfaces cleave the C–O bond of HCOH* to form OH* and CH* (Step 9). Finally, sequential hydrogen addition steps that add three H* successively onto the CH* species form CH_4 (Steps 11A-13A), thus completing the catalytic cycle. This pathway is previously proposed for CO–H_2 reactions from experiments on supported Ni clusters[13] and Ni–Cu alloy films[30] at 523–673 K and from DFT calculations on Ni surfaces {Ni(110),[31] Ni (111),[21,31] Ni(211)[21]}. This mechanism is also consistent with the microscopically reverse CH_4 reforming mechanism, where the first C–H bond activation is kinetically relevant (reverse Step

13A) on Ni clusters that are largely uncovered and contain a small amount of carbonaceous intermediates,[8,9] essentially free of reactive O* species.

In contrast to Pathway A, our recent kinetic, isotopic, and DFT studies of CH_4 reforming on these metal clusters suggest that, when metal surfaces such as those of Ni–Co and Co are partially covered with O*, O* may assist with the initial C–H bond activation of CH_4, forming CH_3* and OH* species (reverse of Step 13B).[9] On these O* covered Ni–Co and Co clusters, the methanation reaction must occur via a final H addition step that inserts the H from the OH* onto the CH_3* (Step 13B), as required by the principle of microscopic reversibility.[32,33] According to the principle, methanation and its reverse methane reforming reaction must occur via the exact same sequence of elementary steps on the same surfaces, but the sequences are in the reverse order from each other. This sequence, called Pathway B, proceeds by H addition steps that transfer the H from OH* onto CO*, forming HCO* and HCOH* (Steps 7B and 8B, respectively), before the dissociation of HCOH* to form CH* (Step 9). The CH* undergoes a series of H additions from the hydrogen in OH* to evolve CH_4 (Steps 11B–13B), completing the catalytic cycle.

In both of these pathways, we propose that the final H additions into CH_3* (Step 13*i*) are kinetically relevant, and the H addition steps (Steps 7*i*, 8*i*, 11*i*, 12*i*) prior to Step 13*i*, the C–O cleavage (Step 9) step, and steps related to the RWGS (Steps 1–5) are all quasi-equilibrated, based on the approximately second order dependence of CH_4 rates on the H_2 pressure (Section S4 of the Supporting Information). DFT calculations on Co(0001) and Fe(110) show that the proposed pathway in Scheme 1 is the most energetically favorable C–O cleavage route.[22] We note that the quasi-equilibrated H addition steps (Steps 7*i*, 8*i*, 11*i*, 12*i*) are kinetically irrelevant and may proceed via a different sequence, but nevertheless, any sequence in this part of the catalytic cycle would lead to the same rate expression (e.g., CO* dissociation followed by H addition into C*), because only the initial and final states matter at chemical equilibrium. We also note that Pathway A involves the H* adatoms and Pathway B the hydrogen atoms from the OH* intermediates as the reactive hydrogen species; the hydrogen in the OH* likely acquires proton characters and its transfer may be characterized as a proton transfer step.[9]

The resulting forward rate of methanation ($r_{CH_4,f}$, Equation 11), by considering both the CH_3*–H* (Step 13A) and CH_3*–OH* (Step 13B) reactions that involve the H* adatoms and OH* species, respectively, is (derivation in Supporting Information, Section S3):

$$r_{CH_4,f} = \frac{\overbrace{k_{13A,f}K_{CH_3-H}[H_2]^2\gamma_C}^{\text{PathwayA}} + \overbrace{k_{13B,f}K_{CH_3-OH}[H_2]^2[CO]}^{\text{PathwayB}}}{(1 + \underbrace{K_V\gamma_C}_{C^*} + \underbrace{K_I\gamma_O}_{O^*})^2} \qquad (11)$$

where $k_{13A,f}$ and $k_{13B,f}$ are the forward rate constants for Steps 13A and 13B, and K_{CH_3-H} $(K_1^{-1}K_2^{-2}K_3^2K_4^{-1}K_{7A}K_{8A}K_9K_{11A}K_{12A})$ and K_{CH_3-OH} $(K_2^{-1}K_3^2K_4^4K_{7B}K_{8B}K_9K_{11B}K_{12B})$ are the effective equilibrium coefficients for CH_3*–H* and CH_3*–OH* formation, respectively. The numerator terms of the rate expression give the rates of CH_4 formation via Pathways A and B, whereas the denominator terms reflect the relative abundances of C* or O* to the unoccupied sites (*), as denoted adjacent to the respective terms. This rate expression captures the kinetic phenomena on the Ni, Ni–Co, and Co clusters, from saturated with C*, to uncovered, and then to saturated with O*. In the next section, we show the simplified form of this rate expression for Ni and Ni–Co clusters, which prevails when cluster surfaces are free of O* and partially covered with C* and then we present the contrasting case for Ni–Co and Co clusters, which prevails when cluster surfaces are free of C* and partially covered with O*.

Rate Coefficients for Methanation are Functions of γ_C, a Descriptor of Carbon Chemical Potential on Ni and Ni–Co Clusters Partially Covered with Reactive C* Intermediates (Regime A)

At high γ_C values and carbon chemical potentials, carbon begins to deposit on Ni and Ni–Co but not on Co cluster surfaces, because the Ni and Ni–Co clusters have more negative ΔBE_{C-O} values (Eqn. 2) and thus exhibit higher affinities to carbon than to oxygen (Figure 4). On these clusters, Pathway A becomes the predominant route for methanation and it occurs on surfaces partially or completely covered with carbon, without detectable O* species at large γ_C (>8 kPa on Ni and >6 kPa on Ni–Co) and small γ_O (<1 on Ni and <0.4 on Ni–Co) values. Thus, the $K_V\gamma_C$ term in the denominator of Equation 11 becomes the dominant term and $K_I\gamma_O$ is negligible. These conditions prevail for Ni clusters when the γ_C-to-γ_O ratio, which reflects the ratio of carbon-to-oxygen chemical potential, exceeds 8 kPa (γ_C >8 kPa, γ_O <1) at 873 K, as also independently confirmed from C* and O* chemical titrations (Figures 2–4). On Ni–Co clusters, which have a less negative ΔBE_{C-O} value and therefore a higher affinity to oxygen rather than carbon species when comparing to Ni clusters, Pathway A prevails at a much more limited range of conditions, occurring when the γ_C-to-γ_O ratio exceeds 13 kPa (γ_C >6 kPa, γ_O <0.4, Figures 2–4) at 873 K. Outside of this limited operating range, O* adatoms begin to occupy metal sites.

We define these operating conditions as Regime A, in which Pathway A prevails. In this regime, the rate expression (Equation 11) simplifies to:

$$\text{Regime A}: \quad r_{CH_4,f} = \frac{k_{13A,f}K_{CH_3-H}[H_2]^2\gamma_C}{(1 + K_V\gamma_C)^2} \qquad (12a)$$

$$\text{Regime A}: \quad k_{A,M} = \frac{r_{CH_4,f}}{[H_2]^2} = \frac{k_{13A,f}K_{CH_3-H}\gamma_C}{(1 + K_V\gamma_C)^2} \qquad (12b)$$

where $k_{A,M}$ ($k_{A,M} = r_{CH_4,f}[H_2]^{-2}$) is the effective rate coefficient in Regime A for metal M (M=Ni or Ni–Co). Figure 5 shows the rate coefficient, $k_{A,Ni}$, measured on Ni clusters under all reaction

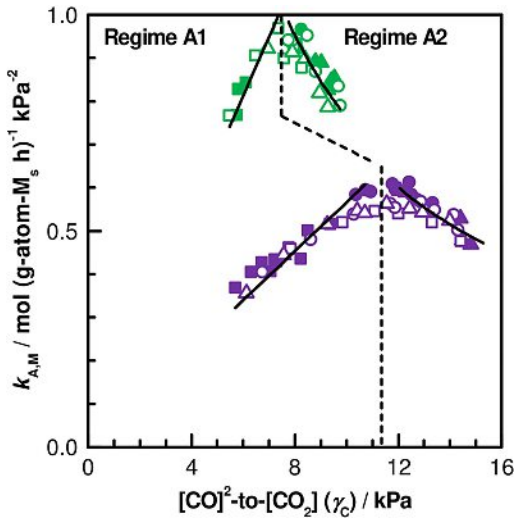

Figure 5. Rate coefficients in Regime A, $k_{A,M}$ ($k_{A,M} = r_{CH_4,f}[H_2]^{-2}$, Eqn. 12b, M is Ni or Ni–Co), plotted as a function of the operating $[CO]^2$-to-$[CO_2]$ (γ_C) ratio, which reflects the carbon chemical potential (Eqn. 10a), during CO_2-H_2 reactions with 5 kPa CO_2 (□, □), 10 kPa CO_2 (○, ○), 15 kPa CO_2 (△, △), 30 kPa H_2 (■, ■), 50 kPa H_2 (●, ●), and 70 kPa H_2 (▲, ▲) on dispersed Ni–Co (for $[CO]^3$-to-$[CO_2]^2$ ratios larger than 7 kPa, □, ○, △, ■, ●, ▲) and Ni (□, ○, △, ■, ●, ▲) clusters at 873 K. Predicted rate coefficients (–) using Equations 13a (Sub-Regime A1) and 13b (Sub-Regime A2) and the parameters in Table 1 are also plotted for comparison with rate data (26–27 nm metal clusters, 12 g-atom% metal on MgO–ZrO_2, 7–14×10^5 cm^3 g_{cat}^{-1} h^{-1}, 10 ZrO_2:catalyst intra-pellet and 100 SiO_2:catalyst inter-pellet dilution ratios).

conditions (19–76 kPa H_2, 2–10 kPa CO_2), as a function of the operating γ_C ratio at 873 K. The $k_{A,Ni}$ values are functions of the operating γ_C ratio and the related carbon chemical potentials (Eqn. 10a). As the γ_C ratio increases, the $k_{A,Ni}$ values first increase linearly in Sub-Regime A1, then reach a plateau at 11 kPa, after which they become inversely proportional to the operating γ_C ratio in Sub-Regime A2. Included in Figure 5 are the rate coefficients for Ni–Co clusters ($k_{A,Ni-Co}$, 873 K), but only for a limited set of conditions when Pathway A prevails ($\gamma_C/\gamma_O = [CO]^3/[CO_2]^2 > 7$ kPa). These $k_{A,Ni-Co}$ values are also functions of the operating γ_C ratio and acquire similar dependencies as $k_{A,Ni}$, i.e., increase linearly and then decrease with the operating γ_C ratios in two distinctly different Sub-Regimes A1 and A2 (γ_C = 5–8 kPa and 8–10 kPa, respectively).

The Sub-Regime A1 prevails when the cluster surfaces are uncovered of C*, when the denominator term $K_V\gamma_C$ in Equation 12b is much smaller than unity ($K_V\gamma_C \ll 1$), under which Equation 12b simplifies to Equation 13a:

$$\text{Sub-Regime A1}: \quad k_{A,M} = k_{13A,f}K_{CH_3-H}\gamma_C \tag{13a}$$

As C* coverages increase to near a monolayer, the denominator term $K_C\gamma_C$ in Equation 12b increases and becomes much larger than unity ($K_V\gamma_C \gg 1$). This leads to the transition to Sub-Regime A2, captured by Equation 13b:

$$\text{Sub-Regime A2}: \quad k_{A,M} = k_{13A,f}K_{CH_3-H}K_V^{-2}\gamma_C^{-1} \tag{13b}$$

The operating γ_C value determines the rate dependencies in Regime A and dictates the transition between the two sub-regimes. Table 2 summarizes the operating γ_C-to-γ_O ratios, $[CO]^3/[CO_2]^2$, for Sub-Regimes A1 and A2. These γ_C-to-γ_O values, obtained from the CO_2–H_2 rate data (Figure 5), agree with those determined from CO–CO_2 titrations (Figure 4).

Non-linear regressions of Equations 13a and 13b against the rate data in Figure 5 for Regime A, which includes both sub-regimes, give the $k_{13A,f}K_{CH_3-H}$ and K_V parameters in Table 1. These parameters describe the methanation reaction kinetics on uncovered and C* covered Ni and Ni–Co clusters. Figure 5 compares the calculated $k_{A,M}$ values from the regression fittings with the measured values, and Figure 6 shows the parity plot between these rate coefficients. These results indicate that the proposed reaction mechanism for Pathway A of Scheme 1 is in good agreement with the measured methanation rates at Ni and Ni–Co clusters with varying C* coverages.

Table 1. Rate and equilibrium parameters determined from non-linear regression of rate data for CO_x-H_2 reactions (Figsures 5 and 8) with the proposed rate equations (Eqns. 13a, 13b, and 14b) on 26–30 nm Ni, Ni–Co, and Co clusters at 873 K.

Catalyst	$k_{13A,f}K_{CH_3-H}$ [kPa^{-3} h^{-1}]	K_V [kPa^{-1}]	$k_{13B,f}K_{CH_3-OH}$ [kPa^{-3} h^{-1}]	K_I [–]
Ni/MgO–ZrO_2	0.057 ± 0.004	0.089 ± 0.012	n.a.	n.a.
Ni–Co/MgO–ZrO_2	0.13 ± 0.01	0.13 ± 0.01	0.50 ± 0.04	0.97 ± 0.08
Co/MgO–ZrO_2	n.a.	n.a.	2.2 ± 0.2	2.0 ± 0.1

n.a. denotes a kinetic regime that is not-applicable to the catalyst.

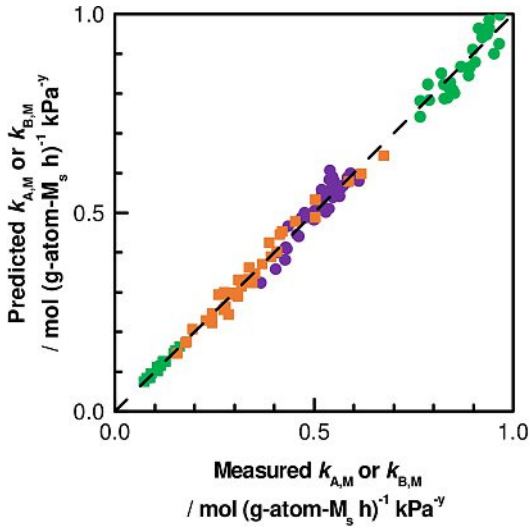

Figure 6. Predicted CO_x methanation rate coefficients in Regimes A (●, ●) and B (■, ■) ($k_{A,M}$ and $k_{B,M}$, where M=Ni, Ni–Co, or Co) from Equations 13a, 13b, and 14b and parameters in Table 1 plotted against the measured rate coefficients on Ni (●), Ni–Co (●, ■), and Co (■) clusters with 3–19 kPa CO_2 and 24–82 kPa H_2 at 873 K (y is 2 for $k_{A,M}$ or 3 for $k_{B,M}$, 27–30 nm clusters, 12 g-atom% metal on MgO–ZrO_2, 7–14×10^5 cm^3 g_{cat}^{-1} h^{-1}, 10 ZrO_2:catalyst intra-pellet and 100 SiO_2:catalyst inter-pellet dilution ratios).

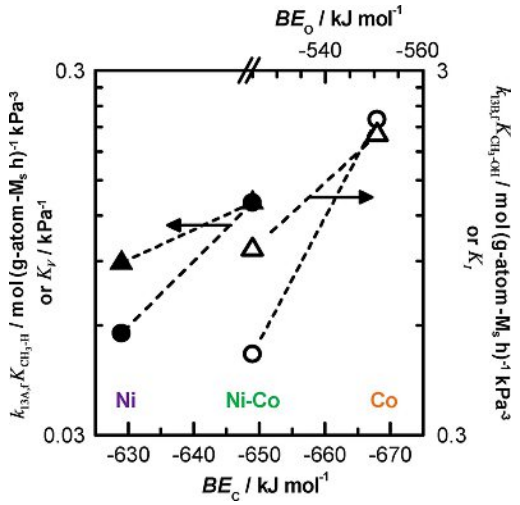

Figure 7. Effective rate coefficients {$k_{13A,f}K_{CH_3-H}$ (●) and $k_{13B,f}K_{CH_3-OH}$ (○)} and equilibrium constants {K_V (▲) and K_I (△)} determined from non-linear regression of CO_x methanation rate data in Regimes A (●, ▲) and B (○, △) at 873 K on 26–30 nm Ni, Ni–Co, and Co clusters (Figures 5 and 8) with the proposed rate equations (Eqns. 13a, 13b, 14b) as a function of the carbon and oxygen binding energies on Ni(111), Ni–Co(111), and Co(111) surfaces.[24]

The $k_{13A,f}K_{CH_3-H}$ and K_V values for Ni and Ni–Co clusters are shown in Figure 7 as a function of their carbon binding energies (BE_C) on (111) terraces.[24] The $k_{13A,f}K_{CH_3-H}$ values on Ni–Co are 2.3 times larger than on Ni; this increase arises from the stronger C* binding energy which results in more stable adsorbates and a higher K_{CH_3-H} value, which reflects the free energy change for the $2CO + 2H_2 + 2^* \rightleftharpoons CH_3^* + H^* + CO_2$ reaction. At the same time, the stronger carbon binding energy also stabilizes the $(H_3C\cdots^*\cdots H)^{\ddagger}$ transition state for Step 13A to a similar extent as the reactant state ($CH_3^* + H^*$), because of the early nature of the transition state,[34] as extracted from DFT calculations on Ni(111) surfaces, which reveal the exothermic nature of Step 13A ($-37\ kJ\,mol^{-1}$).[9] Consequently, $k_{13A,f}$ remains unaffected by the carbon binding energy. Therefore, the larger $k_{13A,f}K_{CH_3-H}$ value on Ni–Co than Ni clusters primarily reflects the stabilization of the CH_3^* adsorbate due to the stronger C* binding on Ni–Co. Similarly, the equilibrium constant of C* formation, K_V (which reflects the free energy change during $2CO + ^* \rightleftharpoons C^* + CO_2$), is 1.5 times larger on Ni–Co than Ni (Figure 7), as a result of the stronger C* binding on Ni–Co.

Rate Coefficients for Methanation are Functions of γ_O, a Descriptor of Oxygen Chemical Potential on Ni–Co and Co Clusters Partially Covered with Reactive O* Intermediates (Regime B)

Next, we examine the kinetic dependencies for CO_x methanation reactions on Ni–Co and Co clusters that retain O* adsorbates instead of C*. This condition occurs for Ni–Co clusters at high oxygen chemical potentials and low carbon chemical potentials, i.e., small γ_C-to-γ_O ratios (<6 kPa, Figure 4). It also occurs on Co clusters over the entire operating range ($\gamma_C/\gamma_O < 32$ kPa). Both Ni–Co and Co clusters exhibit less negative ΔBE_{C-O} values (Eqn. 2) and thus a higher affinity to oxygen rather than carbon, when comparing to Ni. We define these conditions as Regime B, which occurs when cluster surfaces retain O* adatoms rather than C* species. On such surfaces, Pathway B becomes the predominant route, the $K_I\gamma_O$ term in the denominator of Equation 11 becomes the dominant term, while $K_V\gamma_C$ becomes insignificant. As a result, the rate expression (Equation 11) simplifies to:

$$\text{Regime B}: \quad r_{CH_4,f} = \frac{k_{13B,f}K_{CH_3-OH}[H_2]^2[CO]}{(1+K_I\gamma_O)^2} \tag{14a}$$

$$\text{Regime B}: \quad k_{B,M} = \frac{r_{CH_4,f}}{[H_2]^2[CO]} = \frac{k_{13B,f}K_{CH_3-OH}}{(1+K_I\gamma_O)^2} \tag{14b}$$

where $k_{B,M}$ ($k_{B,M} = r_{CH_4,f}[H_2]^{-2}[CO]^{-1}$) is the effective rate coefficient in Regime B for metal M (M=Ni–Co or Co). Figure 8

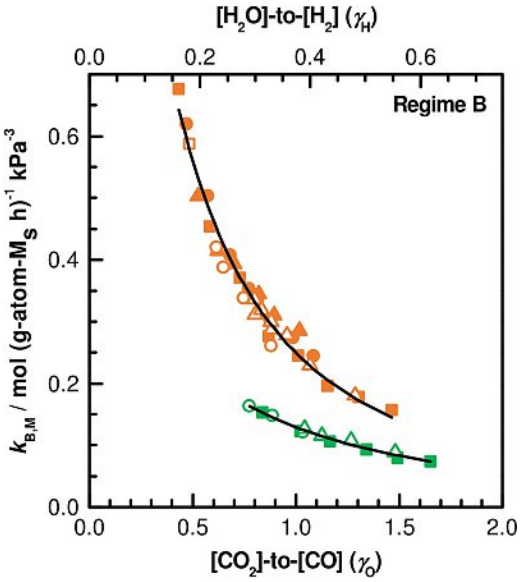

Figure 8. Rate coefficients in Regime B $k_{B,M}$ ($k_{B,M} = r_{CH_4,f}[H_2]^{-2}[CO]^{-1}$, Eqn. 14b, M is Ni–Co or Co) plotted as a function of the operating $[CO_2]$-to-[CO] (γ_O) ratio, which reflects the oxygen chemical potential (Eqn. 7a), during CO_2-H_2 reactions with 5 kPa CO_2 (□, □), 10 kPa CO_2 (○, ○), 15 kPa CO_2 (△, △), 30 kPa H_2 (■, ■), 50 kPa H_2 (●, ●), and 70 kPa H_2 (▲, ▲) on dispersed Co (□, ○, △, ■, ●, ▲) and Ni–Co (for $[CO]^3$-to-$[CO_2]^2$ ratios smaller than 7 kPa, □, ○, △, ■, ●, ▲) clusters at 873 K. Predicted rate coefficients (–) using Equation 14b and the parameters in Table 1 are also plotted for comparison with rate data (27–30 nm metal clusters, 12 g-atom% metal on MgO–ZrO_2, $1.4\times10^6\ cm^3\,g_{cat}^{-1}\,h^{-1}$, 10 ZrO_2:catalyst intra-pellet and 100 SiO_2: catalyst inter-pellet dilution ratios).

confirms that the rate coefficients $k_{B,Ni-Co}$ and $k_{B,Co}$ at 873 K, when operating in this regime, are functions of the operating γ_O and related γ_H ratios (via Eqn. 7a). The $k_{B,Ni-Co}$ and $k_{B,Co}$ values are more than inversely proportional to the operating γ_O ratios, indicating that the $K_I\gamma_O$ term in the denominator of Equation 14b is significant but not dominant and that the O* coverages at the cluster surfaces are between 0.5 and 0.75 ML.

Table 2. Operating γ_C-to-γ_O ratios that prescribe the kinetic regimes and identity of the most abundant surface intermediates during CO_x-H_2 reactions on 26–30 nm Ni, Ni–Co, and Co clusters at 873 K.

Catalyst	C* Covered [Sub-Regime A1] γ_C-to-γ_O [kPa]	Uncovered [Sub-Regime A2] γ_C-to-γ_O [kPa]	O* Covered [Regime B] γ_C-to-γ_O (kPa)
Ni/MgO–ZrO_2	20–67	5–17	n.a.
Ni–Co/MgO–ZrO_2	12–20	7–11	2–7
Co/MgO–ZrO_2	n.a.	n.a.	4–31

n.a. denotes a kinetic regime that is not-applicable to the catalyst.

These results indicate that the MASI in Regime B is O*, and Table 2 summarizes the γ_C-to-γ_O ratios, $[CO]^3/[CO_2]^2$, that lead to these surface coverages on Ni–Co and Co clusters (Figure 8). These γ_C-to-γ_O ratios and the transition from the C* covered, uncovered, to O* covered surfaces derived from rate measurements appear to correlate with those measured by contacting the catalysts to CO-CO_2 mixtures (Figure 4).

Non-linear regression of Equation 14b against the rate data in Figure 8 gives the $k_{13B,f}K_{CH_3-OH}$ and K_I values for methanation reactions on Ni–Co and Co cluster surfaces partially covered with O* adatoms. Table 1 summarizes the rate and equilibrium constant values from the regression, and Figures 6 and 8 compare the calculated to measured $k_{B,M}$ values, which are in strong agreement. These $k_{13B,f}K_{CH_3-OH}$ and K_I values on Ni–Co and Co clusters are plotted against the carbon and oxygen binding energies (BE_C and BE_O) on (111) terraces[24] in Figure 7. Co, a metal that binds to C* and O* much more strongly than Ni–Co, has a $k_{13B,f}K_{CH_3-OH}$ value that is 4.4 times higher. We expect that the CH_3* and OH* intermediates, the reactants in Step 13B (Scheme 1), bind much more strongly on Co than Ni–Co, as their enthalpies of adsorption vary proportionally with the carbon and oxygen binding energies, respectively. For this reason, the K_{CH_3-OH} value, which reflects the free energy change for the $CO + 2H_2 + 2^* \rightleftharpoons CH_3^* + OH^*$ reaction, is larger. Meanwhile, the stronger carbon and oxygen binding energies also stabilize the $(H_3C\cdots*\cdots H\cdots O*)^{\ddagger}$ transition state for Step 13B and thus affect the activation barrier for the reaction. DFT calculations on the (111) terraces of Ni–Co and Co clusters indicate that Step 13B is highly exothermic (−110–−97 kJ mol^{-1}),[9] and therefore, the transition state occurs relatively early along the reaction coordinate. As a result, $k_{13B,f}$ remains relatively insensitive to changes in the carbon and oxygen binding energies as these energies influence the reactant ($CH_3^* + OH^*$) and transition $(H_3C\cdots*\cdots H\cdots O*)^{\ddagger}$ states similarly and do not alter the activation barrier.[34] Consequently, the larger $k_{13B,f}K_{CH_3-OH}$ value on Co than Ni–Co clusters primarily reflects the K_{CH_3-OH} increase because of the stabilization of the CH_3* and OH* adsorbates due to the stronger C* and O* binding energies on Co. The equilibrium constant of O* formation, K_I, which reflects the free energy change during the $CO_2 + * \rightleftharpoons O^* + CO$ reaction, is 2.1 times larger on Co than Ni–Co (Figure 7). This is expected and consistent with the stronger O* binding energy on Co than on Ni–Co.

Conclusions

Rate measurements in the kinetically controlled regime, together with surface oxygen and carbon titrations, lead to a proposed mechanism for CO_x methanation on Ni, Ni–Co, and Co clusters. Under all operating conditions, Ni cluster surfaces remain either uncovered or covered with C* to different extents, without any detectable O* coverages. Comparing to Ni, Ni–Co clusters have a greater affinity to oxygen than carbon. In addition to site occupation by C*, Ni–Co cluster surfaces may instead retain O* at high oxygen-to-carbon chemical potential ratios. Comparing to Ni–Co and Ni, Co cluster surfaces have an even higher relative affinity to oxygen than carbon. As a result, Co cluster surfaces remain partially covered with O*, without any C* deposition for all oxygen-to-carbon chemical potential ratios relevant to methanation catalysis. During steady-state catalysis, the operating $[CO]^2$-to-$[CO_2]$ and $[CO_2]$-to-[CO] pressure ratios are surrogates of the carbon and oxygen chemical potentials, respectively, because the Boudouard and reverse water-gas shift reactions and their pathways that form the C* and O* adsorbates are quasi-equilibrated. These pressure ratios and the thermodynamic properties that they describe determine the identity of the most abundant surface intermediates and the operating kinetic regime.

On cluster surfaces partially covered with C*, which prevail on Ni and, at a subset of operating conditions, on Ni–Co, CH_4 forms from a kinetically relevant hydrogen adatom addition step that adds H* to an adsorbed CH_3* intermediate. In contrast, for cluster surfaces partially covered with O*, found on Co under all conditions and on Ni–Co under a limited set of conditions, CH_4 forms from a kinetically relevant hydrogen addition step that inserts a proton from OH* into a CH_3* intermediate. The different identities of the kinetically relevant step, the most abundant surface intermediate, and the charge of the hydrogen donor lead to distinctly different kinetic dependencies. On cluster surfaces that are predominantly uncovered or covered with C*, the rate coefficients increase linearly or are inversely proportional to the operating $[CO]^2$-to-$[CO_2]$ pressure ratio, respectively. For the contrasting case in which cluster surfaces are predominantly covered with O*, the rate coefficients are inversely proportional to the operating $[CO_2]$-to-[CO] pressure ratio.

Taken together from the kinetic and chemical titration results and thermodynamic considerations, we show that the operating $[CO]^2$-to-$[CO_2]$ ratios relate directly to the carbon chemical potentials, whereas the $[CO_2]$-to-[CO] and the associated $[H_2O]$-to-$[H_2]$ ratios relate directly to the oxygen chemical potentials at cluster surfaces, because the water-gas shift reaction reaches chemical equilibrium. In other words, these ratios are descriptors of the instantaneous C* and O* coverages on these first-row transition metals, and their relations are set by thermodynamics. The relative carbon and oxygen chemical potentials, together with the relative affinity to carbon and oxygen of these clusters, dictate the identity of the most abundant surface intermediates, the charge of the reactive hydrogen in the kinetically relevant hydrogen insertion step, and in turn the rate coefficients and dependencies during

methanation reactions. These effects lead to the observed periodic reactivity trends for methanation on first-row transition metals.

Experimental Section

Synthesis of Supported Ni, Ni–Co, and Co Clusters Dispersed on MgO-ZrO_2 Particles

A MgO-ZrO_2 (MgO:ZrO_2 molar ratio of 5:2) support was prepared by co-precipitation. A solution of 0.70 M $Mg(NO_3)_2$ and 0.28 M ZrO$(NO_3)_2$ was prepared by dissolving $Mg(NO_3)_2 \cdot 6H_2O$ (Sigma-Aldrich, 99%) and $ZrO(NO_3)_2 \cdot 6H_2O$ (Sigma-Aldrich, 99%) in doubly deionized water (>18.2 MΩ cm) at 333 K under constant stirring. A solution of 2.0 M $(NH_4)_2CO_3$ (Sigma-Aldrich, ACS reagent) in doubly deionized water was added to the $Mg(NO_3)_2$ and $ZrO(NO_3)_2$ solution dropwise while maintaining the temperature at 333 K until the pH reached 9.5 ± 0.5 (approximately 5 h), during which the precipitate formed. The suspension was cooled to ambient temperature and then filtered (Fisher filter paper, particle retention >20 μm). The precipitate was treated in stagnant ambient air at 393 K for 12 h and then in flowing dry air (Linde, 99.999%) at 0.5 $cm^3 g^{-1} s^{-1}$ by heating at 0.05 $K s^{-1}$ to 1073 K and holding isothermally for 5 h.

Supported Ni, Co, and Ni–Co catalysts were prepared via impregnation of the MgO-ZrO_2 supports with metal precursor solutions. Aqueous solutions of $Ni(NO_3)_2 \cdot 6H_2O$ (Sigma-Aldrich, 99.999%), Co$(NO_3)_2 \cdot 6H_2O$ (Sigma-Aldrich, 99.999%), or both precursors were dissolved in doubly deionized water. These solutions were impregnated onto the MgO-ZrO_2 supports (2 $cm^3 g_{support}^{-1}$) to form 12 g-atom% Ni, 12 g-atom% Co, or 6 g-atom% Ni and 6 g-atom% Co catalysts, which are denoted herein as Ni, Co, or Ni–Co, respectively, as shown in Table 3. The samples were treated in stagnant ambient air at 393 K for 12 h. Next, the samples were treated in flowing 5% H_2 (5.22% H_2 in He, Linde certified standard) at 0.5 $cm^3 g^{-1} s^{-1}$ by heating at 0.03 $K s^{-1}$ to 1023 K and holding isothermally for 2 h. The resulting catalyst powders were mixed with ZrO_2 (Sigma-Aldrich, 99%, 0–5 μm) at intra-particle ZrO_2-to-catalyst dilution mass ratios of 5:1, 10:1, and 20:1. The mixtures were pelletized with a hydraulic press (Specac) using a pellet die (Carver, 31 mm ID) at 130 MPa for 0.5 h and the resulting disc was crushed and sieved to obtain 125–180 μm particles.

Table 3. Catalyst metal loadings, dispersions, and mean cluster diameters.

Catalyst Name	Ni Loading (g-atom%)	Co Loading (g-atom%)	Dispersion	Mean Cluster Diameter (nm)
Ni/MgO–ZrO_2	12	0	0.039	26
Ni–Co/MgO–ZrO_2	6	6	0.037	27
Co/MgO–ZrO_2	0	12	0.033	30

Isothermal H_2 Uptakes and Surface Oxygen and Carbon Measurements on Metal Clusters

Isothermal volumetric H_2 uptakes were carried out at 313 K in an adsorption-desorption apparatus (10.6 cm^3 STP gas manifold and 11.4 cm^3 STP reaction chamber) equipped with a pressure transducer (MKS, 120AA Baratron, dual ranges of 0–13 and 0–133 kPa, 0.1% accuracy), vacuum turbopump (Pfeiffer, HiPace 80), diaphragm pump (Pfeiffer, MVP 015–2), 6-way valve (Valco Instruments), and thermal mass flow controllers (Brooks, SLA5850). The catalyst samples were loaded into a quartz sample holder and treated in flowing H_2 (0.5 $cm^3 g^{-1} s^{-1}$, Linde, 99.999%) by heating at 0.03 $K s^{-1}$ to 1023 K and then held for 2 h at 1023 K. Next, the sample holder and manifold were evacuated under dynamic vacuum (10^{-5} Pa) for 12 h at 1023 K prior to cooling to 313 K at 0.03 $K s^{-1}$. Two consecutive H_2 uptake isotherms were measured at 313 K over the pressure range of 0–13 kPa by introducing doses of 2–16 μmol H_2 from the gas manifold to the reaction chamber in 0.08 h time intervals, and the sample was evacuated under dynamic vacuum for 0.5 h between these isotherm measurements. The fraction of exposed surface metal atoms and the average cluster diameters were determined by the difference between the extrapolated values from the two H_2 isotherms at zero H_2 pressure,[35] by assuming an atomic ratio of surface H-to-surface metal of unity ($H_s/M_s = 1$, subscript *s* denotes surface atoms)[35] and that the metal clusters are hemispherical with their density similar to their respective bulk structure (8.90 g cm^{-3} for Co, 8.91 g cm^{-3} for Ni, and 8.91 g cm^{-3} for Ni–Co[36]). The metal cluster dispersions and average cluster diameters are summarized in Table 3.

Equilibrium coverages of oxygen adatoms (O*) at metal cluster surfaces, when contacting the catalysts to CO_2, were quantified using the same volumetric adsorption-desorption apparatus. A catalyst sample was treated in flowing H_2 (0.5 $cm^3 g^{-1} s^{-1}$) by heating at 0.03 $K s^{-1}$ to and holding for 2 h at 1023 K. The sample was then evacuated under dynamic vacuum for 12 h at 1023 K before cooling to 873 K. A CO_2 dose (25–500 μmol, Linde, 99.99%) was introduced into the reaction chamber. After 2 h, a dose of the resulting gas mixture, which contains CO and CO_2, was withdrawn from the chamber through the 6-way valve and then analyzed with gas chromatograph (SRI, 8610C) equipped with a HayeSep D (SRI, 6′×1/8″SS) packed column connecting to a micro-methanizer and then to a flame ionization detector (FID). The amount of CO, which was formed from CO_2 decomposition (Step I, Scheme 1), together with the surface density of metal atoms, was used to determine the O* coverages.

Equilibrium C* coverages at metal cluster surfaces upon contacting to CO–CO_2 mixtures were measured with sequential temperature programmed oxidation. A catalyst sample was treated in flowing H_2 (0.5 $cm^3 g^{-1} s^{-1}$), by heating at 0.03 $K s^{-1}$ to and holding for 2 h at 1023 K. Flowing Ar (Linde, 99.999%, 0.5 $cm^3 g^{-1} s^{-1}$) was then introduced for 0.5 h before cooling the sample to 873 K. Next, a mixture with the targeted CO:CO_2 ratio (0.5–4) was prepared by metering the individual gas flowrates of CO (5.09% CO in Ar, Linde certified standard), CO_2 (Linde, 99.99%), and Ar (Linde, 99.999%) with thermal mass flow controllers (Brooks, SLA5850) and introduced to the sample. After 4 h, flowing Ar (0.5 $cm^3 g^{-1} s^{-1}$) was introduced to the sample for 0.5 h before cooling the sample from 873 K to ambient temperature. Next, a stream containing 1% O_2, prepared by mixing diluted O_2 (5.05% O_2 in He, Linde certified standard) and Ar, was introduced to the sample while heating at 0.08 $K s^{-1}$ to 1073 K. The reactor effluent was mixed with H_2 (Linde, 99.999%) and passed through a methanizer prior to being continuously analyzed with a FID (SRI).

CH_4 Formation Rates and Approach-to-Equilibrium for Methanation and Reverse Water-Gas Shift Reactions with CO_2-H_2 Mixtures

Rates of CO_2-H_2 were measured in a fixed bed microcatalytic quartz reactor (8.1 mm ID). Catalyst pellets (125–180 μm) were mixed with SiO_2 (SiO_2, Sigma-Aldrich, purum p.a., 125–180 μm) at inter-particle SiO_2-to-catalyst dilution mass ratios of 50:1 and 100:1 and were supported by a quartz frit inside the tubular quartz reactor. These

pellets were treated in flowing H_2 (Linde, 99.999%) by heating at 0.05 K s^{-1} to 1023 K and holding isothermally for 2 h. Next, Ar (Linde, 99.999%) was introduced for 0.5 h before cooling to 873 K. Thermal mass flow controllers (Brooks, SLA5850) were used to meter individual reactant gases of CO_2 (Linde certified standard, 99.99%), H_2 (Linde, 99.999%), and Ar (Linde, 99.999%) independently. All gas transfer lines were kept above 333 K such that H_2O (< 20 kPa) remained in the vapor phase. The reactor effluent passed through a H_2O trap prior to analysis using a gas chromatograph (SRI, 8610C) equipped with molecular sieve 13X (SRI, 6′×1/8″SS) and HayeSep D (SRI, 6′×1/8″ SS) packed columns connected in series (with an optional bypass around the molecular sieve 13X column) that led to a thermal conductivity detector (TCD) followed by a micro-methanizer and then an FID.

Acknowledgements

This work was supported by the Natural Sciences and Engineering Research Council of Canada and the Canada Foundation for Innovation. P. T. L. acknowledges the support of the Queen Elizabeth II Graduate Scholarships in Science & Technology and the Ontario Graduate Scholarships. We thank Weifeng Tu for synthesizing and characterizing the Ni, Ni–Co, and Co clusters.

Conflict of Interest

The authors declare no conflict of interest.

Keywords: methanation · transition metal cluster · hydrogen addition · periodic trend · chemisorbed oxygen

[1] J. Gao, Q. Liu, F. Gu, B. Liu, Z. Zhong, F. Su, *RSC Adv.* **2015**, *5*, 22759–22776.
[2] M. P. Andersson, F. Abild-Pedersen, I. N. Remediakis, T. Bligaard, G. Jones, J. Engbæk, O. Lytken, S. Horch, J. H. Nielsen, J. Sehested, *J. Catal.* **2008**, *255*, 6–19.
[3] G. A. Mills, F. W. Steffgen, *Catal. Rev.* **1974**, *8*, 159–210.
[4] A. T. Bell, *Catal. Rev.* **1981**, *23*, 203–232.
[5] E. Iglesia, *Appl. Catal. Gen.* **1997**, *161*, 59–78.
[6] J. Sehested, K. E. Larsen, A. L. Kustov, A. M. Frey, T. Johannessen, T. Bligaard, M. P. Andersson, J. K. Nørskov, C. H. Christensen, *Top. Catal.* **2007**, *45*, 9–13.
[7] S. Takenaka, T. Shimizu, K. Otsuka, *Int. J. Hydrogen Energy* **2004**, *29*, 1065–1073.
[8] J. Wei, E. Iglesia, *J. Catal.* **2004**, *224*, 370–383.
[9] W. Tu, M. Ghoussoub, C. V. Singh, Y.-H. (Cathy) Chin, *J. Am. Chem. Soc.* **2017**, DOI 10.1021/jacs.7b01632.
[10] D. W. Goodman, R. D. Kelley, T. E. Madey, J. T. Yates, *J. Catal.* **1980**, *63*, 226–234.
[11] J. Xu, G. F. Froment, *AIChE J.* **1989**, *35*, 88–96.
[12] T. Bligaard, J. K. Nørskov, S. Dahl, J. Matthiesen, C. H. Christensen, J. Sehested, *J. Catal.* **2004**, *224*, 206–217.
[13] J. Sehested, S. Dahl, J. Jacobsen, J. R. Rostrup-Nielsen, *J. Phys. Chem. B* **2005**, *109*, 2432–2438.
[14] H. Habazaki, M. Yamasaki, B.-P. Zhang, A. Kawashima, S. Kohno, T. Takai, K. Hashimoto, *Appl. Catal. Gen.* **1998**, *172*, 131–140.
[15] M. P. Andersson, T. Bligaard, A. Kustov, K. E. Larsen, J. Greeley, T. Johannessen, C. H. Christensen, J. K. Nørskov, *J. Catal.* **2006**, *239*, 501–506.
[16] A. L. Kustov, A. M. Frey, K. E. Larsen, T. Johannessen, J. K. Nørskov, C. H. Christensen, *Appl. Catal. Gen.* **2007**, *320*, 98–104.
[17] S. K. Beaumont, S. Alayoglu, C. Specht, W. D. Michalak, V. V. Pushkarev, J. Guo, N. Kruse, G. A. Somorjai, *J. Am. Chem. Soc.* **2014**, *136*, 9898–9901.
[18] P. Panagiotopoulou, D. I. Kondarides, X. E. Verykios, *Appl. Catal. Gen.* **2008**, *344*, 45–54.
[19] S. Eckle, Y. Denkwitz, R. J. Behm, *J. Catal.* **2010**, *269*, 255–268.
[20] F. Masini, C. E. Strebel, D. N. McCarthy, A. U. F. Nierhoff, J. Kehres, E. M. Fiordaliso, J. H. Nielsen, I. Chorkendorff, *J. Catal.* **2013**, *308*, 282–290.
[21] H. S. Bengaard, J. K. Nørskov, J. Sehested, B. S. Clausen, L. P. Nielsen, A. M. Molenbroek, J. R. Rostrup-Nielsen, *J. Catal.* **2002**, *209*, 365–384.
[22] M. Ojeda, R. Nabar, A. U. Nilekar, A. Ishikawa, M. Mavrikakis, E. Iglesia, *J. Catal.* **2010**, *272*, 287–297.
[23] B. T. Loveless, C. Buda, M. Neurock, E. Iglesia, *J. Am. Chem. Soc.* **2013**, *135*, 6107–6121.
[24] R. A. Van Santen, M. Neurock, *Molecular Heterogeneous Catalysis*, Wiley-VCH, Weinheim; Chichester, **2006**.
[25] J. Greeley, M. Mavrikakis, *J. Phys. Chem. B* **2005**, *109*, 3460–3471.
[26] M. Boudart, *J. Phys. Chem.* **1983**, *87*, 2786–2789.
[27] C. Kemball, *Discuss. Faraday Soc.* **1966**, *41*, 190–199.
[28] S. Wang, B. Temel, J. Shen, G. Jones, L. C. Grabow, F. Studt, T. Bligaard, F. Abild-Pedersen, C. H. Christensen, J. K. Nørskov, *Catal. Lett.* **2011**, *141*, 370–373.
[29] S. Wang, V. Petzold, V. Tripkovic, J. Kleis, J. G. Howalt, E. Skúlason, E. M. Fernández, B. Hvolbæk, G. Jones, A. Toftelund, *Phys. Chem. Chem. Phys.* **2011**, *13*, 20760–20765.
[30] M. Araki, V. Ponec, *J. Catal.* **1976**, *44*, 439–448.
[31] J. L. C. Fajín, J. R. B. Gomes, M. N. D. S. Cordeiro, *J. Phys. Chem. C* **2015**, *119*, 16537–16551.
[32] R. C. Tolman, *The Principles of Statistical Mechanics*, Courier Corporation, **1938**.
[33] G. N. Lewis, *Proc. Mont. Acad. Sci.* **1925**, *11*, 179–183.
[34] R. A. Van Santen, M. Neurock, S. G. Shetty, *Chem. Rev.* **2010**, *110*, 2005–2048.
[35] G. Bergeret, P. Gallezot, in *Handb. Heterog. Catal.*, Wiley-VCH, Weinheim, **2008**, pp. 738–765.
[36] D. R. Lide, *CRC Handbook of Chemistry and Physics*, CRC Press, Boca Raton, Florida, **1997**.

Manuscript received: September 20, 2018
Revised manuscript received: December 6, 2018
Accepted manuscript online: December 10, 2018
Version of record online: January 30, 2019